ATLAS NOTE

ATLAS-CONF-2015-031

27th July 2015

Measurements of four-lepton production in pp collisions at $\sqrt{s} = 8$ TeV with the ATLAS detector

The ATLAS Collaboration

Abstract

The four-lepton (4ℓ, $\ell = e, \mu$) production is measured in a mass range from 80 to 1000 GeV using 20.3 fb^{-1} of data in pp collisions at $\sqrt{s} = 8$ TeV at the LHC with the ATLAS detector. The 4ℓ signal events come from the decays of resonant Z and Higgs bosons and the non-resonant ZZ continuum produced from $q\bar{q}$, gg, and qg initial states. A total of 476 signal candidate events is observed with a background expectation of 26.2 ± 3.6 events, enabling the measurement of the integrated cross section and the differential cross section as a function of the invariant mass and transverse momentum of the four-lepton system.

In the mass range above 180 GeV, assuming the theoretical constraint on the $q\bar{q}$ production cross section calculated with perturbative next-to-next-to leading order (NNLO) QCD and next-to-leading order (NLO) Electroweak corrections, the signal strength of the gluon-fusion component with respect to the leading order (LO) prediction is determined to be $\mu_{gg} = 2.4 \pm 1.0(\text{stat.}) \pm 0.5(\text{syst.}) \pm 0.8(\text{theory})$.

ATLAS-CONF-2015-031
27 July 2015

1 Introduction

This paper presents measurements of the 4ℓ ($\ell = e, \mu$) production cross section including both the integrated cross section and the spectra of the invariant mass and the transverse momentum of the 4ℓ system, $m_{4\ell}$ and $p_T^{4\ell}$, which are all unfolded to the particle level. In addition, the signal strength of gluon fusion (ggF) production with respect to its leading-order (LO) QCD estimation is measured. This is performed using 20.3 fb^{-1} of data in proton–proton collisions at a centre-of-mass energy of $\sqrt{s} = 8$ TeV from the ATLAS detector at the LHC. The 4ℓ signal events come from the decays of resonant Z and Higgs bosons and the non-resonant ZZ continuum produced from $q\bar{q}$, gg, and qg initial states. These measurements test the validity of the Standard Model (SM) through the interplay of QCD and Electroweak effects for different 4ℓ production mechanisms.

The production mechanisms of the 4ℓ signal events are briefly discussed below.

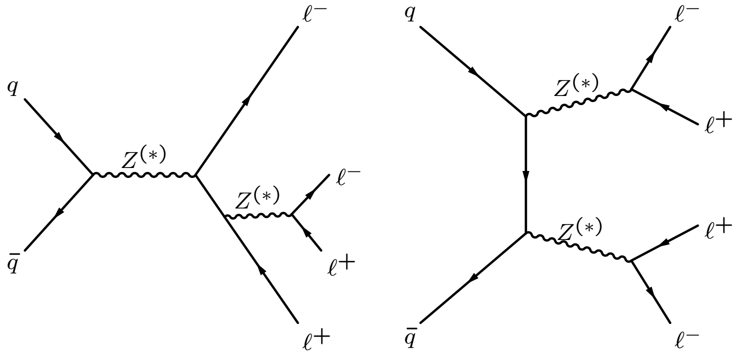

(a) (b)

Figure 1: The LO Feynman diagrams for the $q\bar{q}$-initiated production of 4ℓ: (a) s-channel production of $q\bar{q} \to Z^{(*)} \to \ell^+\ell^-$ with associated radiative decays to an additional lepton pair; (b) t-channel production of $q\bar{q} \to Z^{(*)}\,Z^{(*)} \to 4\ell$.

• $q\bar{q}$-originated 4ℓ production

The tree-level diagrams for $q\bar{q} \to 4\ell$ production are shown in Figure 1 and the cross section as a function of $m_{4\ell}$ is shown in Figure 2. The $Z^{(*)}$ notation means $Z/Z^*/\gamma^*$. The 4ℓ events at the Z resonance occurs predominantly via the s-channel diagram as shown in Figure 1(a), and has been previously measured by the ATLAS and CMS collaborations [3, 4]. In the 4ℓ invariant mass region above the Z-resonance the 4ℓ event production mainly proceeds through the t-channel process as shown in Figure 1(b). The cross section significantly increases when both Z bosons are produced on-shell, resulting in the rise in the $m_{4\ell}$ spectrum around 180 GeV. The $q\bar{q} \to ZZ \to 4\ell$ production via vector-boson scattering (VBS) is also considered as a 4ℓ signal.

• ***4ℓ* *from Higgs boson decays***

Figure 3(a) shows the diagram for the dominant Higgs-boson production mechanism via ggF. Other Higgs-boson production mechanisms, vector-boson fusion (VBF), vector-boson associate production (VH), and top-pair associated production ($t\bar{t}H$), provide less than 15 % 4ℓ events from on-shell Higgs boson decays to $ZZ^{(*)}$. The on-shell Higgs-boson production and decay leads to a sharp resonance around 125 GeV, which is a key signature in the Higgs-boson discovery by the ATLAS [5] and CMS [6] collaborations. The off-shell Higgs-boson production has large destructive interference with the continuum ZZ production from the ggF processes [7–9]. This effect can be observed in the distributions shown in Figure 2, and has

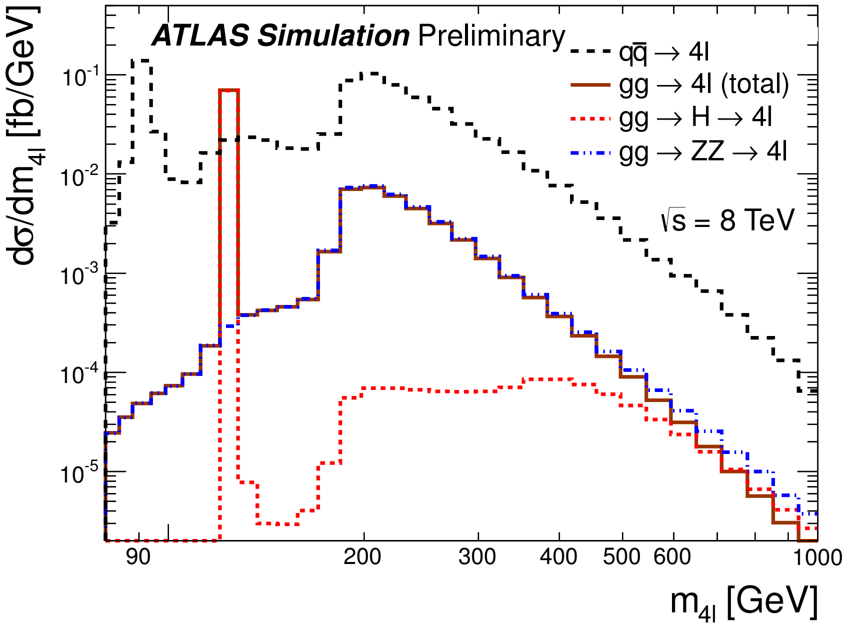

Figure 2: The differential cross sections, $d\sigma/dm_{4\ell}$ vs. $m_{4\ell}$, calculated by MCFM [1] from the $q\bar{q}$ and gg initial states at 8 TeV for the $2e2\mu$ final state in the ATLAS experimental fiducial phase space. The inclusive $gg \to 4\ell$ distribution is the sum of the $gg \to H \to 4\ell$ and the $gg \to ZZ \to 4\ell$ plus interference terms. The calculation of the $q\bar{q} \to 4\ell$ differential production cross section, includes perturbative QCD corrections at NLO, while the distributions from the gg initial state are calculated at the LO. The NNLO K-factors [2] are applied to on-shell Higgs boson production.

been used as a tool to constrain the total Higgs-boson width by the ATLAS and CMS collaborations [10, 11].

- *Non-resonant $\boldsymbol{ZZ \to 4\ell}$ production via $\boldsymbol{ggF}$, $\boldsymbol{VBF}$ and $\boldsymbol{VBS}$ processes*

The non-resonant $ZZ \to 4\ell$ production via ggF, VBF and VBS processes include the production of off-shell Higgs bosons and continuum ZZ as well as their interference. Figure 3(b) shows the non-resonant ZZ production process from ggF. This process produces a sizable number of 4ℓ events in $m_{4\ell} > 2 \times m_Z$ mass region and dominates the total gluon-initiated 4ℓ production. Currently, the gluon-fusion production is less well estimated theoretically with only a LO QCD prediction for the gg continuum production [8, 12].

Contributions from different processes have different strength as a function of $m_{4\ell}$ (Figure 2) and $p_T^{4\ell}$. Therefore, integrated and differential 4ℓ production cross sections are measured as a function of $m_{4\ell}$ and $p_T^{4\ell}$. This is first performed in the experimental fiducial phase space, and then extended to a common phase space for three 4ℓ channels: $4e$, 4μ, and $2e2\mu$. The mass range above 180 GeV is used to determine the signal strength of the gluon-fusion component with respect to its LO prediction. This is done by fitting the observed $m_{4\ell}$ spectrum using the NNLO QCD theoretical prediction, corrected for NLO electroweak effects, for the production originating from the $q\bar{q}$ initial state.

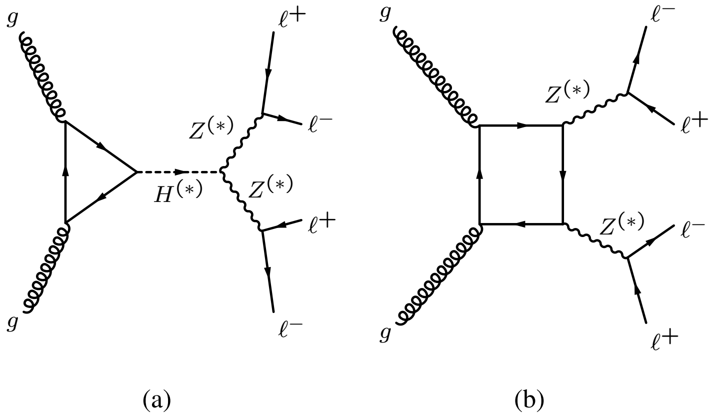

(a) (b)

Figure 3: The tree-level Feynman diagrams for the gg-initiated production of 4ℓ: (a) Higgs boson production through gluon-fusion $gg \to H^{(*)} \to ZZ^{(*)} \to 4\ell$; (b) non-resonant 4ℓ production through quark-box diagram $gg \to Z^{(*)} Z^{(*)} \to 4\ell$.

2 The ATLAS Detector

The ATLAS detector [13] has a cylindrical geometry[1] and consists of an inner tracking detector (ID) surrounded by a 2 T superconducting solenoid, electromagnetic and hadronic calorimeters, and a muon spectrometer (MS) with a toroidal magnetic field. The ID provides tracking for charged particles for $|\eta| < 2.5$. It consists of silicon pixel and strip detectors surrounded by a straw tube tracker that also provides transition radiation measurements for electron identification. The electromagnetic and hadronic calorimeter system covers the pseudorapidity range $|\eta| < 4.9$. For $|\eta| < 2.5$, the liquid-argon electromagnetic calorimeter is finely segmented and plays an important role in electron identification. The MS includes fast trigger chambers ($|\eta| < 2.4$) and high-precision tracking chambers covering $|\eta| < 2.7$. A three-level trigger system selects events to be recorded for offline physics analysis.

3 Signal and background simulation

The signal modelling for $q\bar{q} \to 4\ell$ production uses the POWHEG-BOX Monte Carlo (MC) program [14–16], which includes perturbative QCD corrections at NLO. The production through the qg initial state is included in the NLO calculations. The CT10NLO [17] set of parton distribution functions (PDFs), with QCD renormalisation and factorization scales ($\mu_{\mathrm{R}}, \mu_{\mathrm{F}}$) set to $m_{4\ell}$ are used to calculate the cross section and generate the kinematic distributions. The NNLO QCD [18] and the NLO Electroweak (EW) [19] corrections are applied to the NLO cross section calculated by POWHEG-BOX as a function of the 4ℓ mass for the kinematic region where both Z bosons are produced on-shell. Following the same approach described in Ref. [10], the 4ℓ event distributions are re-weighted to match those expected when using QCD scales of $m_{4\ell}/2$. This is done to unify the QCD scales used in the simulation of the $q\bar{q}$ and the gg processes.

---

[1] ATLAS uses a right-handed coordinate system with its origin at the nominal interaction point (IP) in the centre of the detector, and the z-axis along the beam line. The x-axis points from the IP to the centre of the LHC ring, and the y-axis points upwards. Cylindrical coordinates (r, ϕ) are used in the transverse plane, ϕ being the azimuthal angle around the beam line. The pseudorapidity is defined in terms of the polar angle θ as $\eta = -\ln\tan(\theta/2)$. Observables labelled "transverse" are projected into the x–y plane.

The signal modelling of the on-shell Higgs-boson production via ggF and VBF mechanisms uses POWHEG-BOX which provides calculations at NLO QCD, with the CT10NLO PDFs and μ_{R}, $\mu_{\mathrm{F}} = m_{4\ell}$. The Higgs-boson production via VH and $t\bar{t}H$ mechanisms is simulated with PYTHIA8 [20]. The NNLO QCD and NLO EW effects on the cross-section calculations for on-shell Higgs-boson production are summarized in Ref. [21]. The expected event yields of on-shell Higgs boson are normalised with the higher-order corrected cross sections.

The non-resonant 4ℓ signal production includes off-shell Higgs-boson production, continuum ZZ production, and their interference. The LO MCFM generator is used to simulate the non-resonant ggF production, with the CT10NNLO [22] set of PDFs with QCD scales of μ_{R}, μ_{F} set to $m_{4\ell}/2$; while the LO MADGRAPH generator [23] is used to simulate the non-resonant VBF and VBS productions and their interference. The NNLO QCD corrections are available for the off-shell Higgs-boson production [2] and for the interference between the off-shell Higgs boson and the ZZ production from the gg initial state [24]. However, no higher-order corrections are available for the continuum $gg \to ZZ$ process, which dominates the 4ℓ events from the gg initial state in the region outside the Higgs boson resonance. Therefore, the LO cross section is used for the normalisation of the 4ℓ events produced in gluon-fusion processes.

All the signal MC generators are interfaced to PYTHIA8 for parton shower simulation, except MADGRAPH, which is interfaced to PYTHIA6 [25].

Backgrounds in this analysis include reconstructed 4ℓ events from Z+jets, $t\bar{t}$, diboson (ZW, $Z\gamma$ and double-DY), triboson VVV ($V = Z, W$) and,$VH(H \to VV)$, and Z+top ($t\bar{t}$ and t) processes, which are also simulated.

The reducible background from Z + jets production, that includes light and heavy flavour contributions, is modelled using both SHERPA [26] and ALPGEN [27]. The $Z\gamma$ process is simulated with SHERPA. The $t\bar{t}$ background is modelled using POWHEG-BOX.

Background events from ZH production, where $Z \to \ell\ell$ and $H \to VV$ (VV= WW or ZZ with two leptons and two neutrinos or two leptons and two jets in the final state), are simulated with PYTHIA8. The ZW and the tZ processes are simulated with SHERPA and MADGRAPH respectively. The irreducible background from VVV and $t\bar{t}Z$ is modelled with MADGRAPH. Finally, the double-Drell-Yan ZZ production is modelled with PYTHIA8.

The POWHEG-BOX, MADGRAPH and MCFM generators are interfaced to PYTHIA8 for the parton shower, hadronization and underlying event simulation. The ALPGEN generator is interfaced to HERWIG [28] for the parton shower and to JIMMY [29] for the underlying event simulation. SHERPA uses built–in models for both parton shower and underlying event description.

Both signal and background MC events are simulated using the ATLAS detector simulation [30] based on the GEANT4 [31] framework. Additional pp interactions in the same and nearby bunch crossings (pile-up) are included in the simulations. The MC samples are re-weighted to reproduce the observed distribution of the mean number of interactions per bunch crossing observed in the data.

4 Event Reconstruction and Selection

The following event selection criteria are applied to the events collected with a single-lepton or di-lepton trigger. The transverse momentum and transverse energy thresholds for the single-muon and single-electron triggers are 24 GeV. Two dimuon triggers are used, one with symmetric thresholds at 13 GeV and the other with asymmetric thresholds at 18 GeV and 8 GeV. For the dielectron trigger the symmetric thresholds are 12 GeV. Furthermore there is an electron-muon trigger with thresholds at 12 GeV (electron) and 8 GeV (muon).

A primary vertex reconstructed from at least three well-reconstructed charged particle tracks, each with $p_T > 0.4$ GeV is required in order to remove non-collision background and ensure good object reconstruction. For events with more than one primary vertex, the vertex with the largest $\sum p_T^2$ of the associated tracks is selected.

Electron candidates are reconstructed from a combination of a cluster of energy deposits in the electromagnetic calorimeter and a track in the ID. They are required to have $p_T > 7$ GeV and $|\eta| < 2.47$. Candidate electrons must satisfy a loose set of identification criteria based on a likelihood built from parameters characterizing the shower shape and track association as described in Ref. [32].

Muon identification is performed according to several criteria based on the information from the ID, the MS, and the calorimeter sub-detector systems. The different types of reconstructed muons are: a) Combined (CB), which is the combination of tracks reconstructed independently in the ID and MS; b) Stand-Alone (SA), where the muon trajectory is reconstructed only in the MS; c) Segment-tagged (ST), where a track in the ID is associated with at least one local track segment in the MS; and d) Calorimeter-tagged (CaloTag), where a track in the ID is identified as a muon if it is associated to a minimum ionizing particle energy deposit in the calorimeter system.

The acceptance coverage range for both CB and ST muons is $|\eta| < 2.5$, while the SA muons are used to extend the $|\eta|$ acceptance from 2.5 to 2.7. which is not covered by the ID. CaloTag muons are used in the rapidity range $|\eta| < 0.1$ where there is incomplete MS coverage. All muon candidates are required to have $p_T > 6$ GeV.

In order to reject electrons and muons from jets, only isolated leptons are selected. Two isolation requirements are used, one for the ID and one for the calorimeter. For the ID, the requirement is that the scalar sum of the transverse momenta, $\sum p_T$, of all tracks inside a cone of $\Delta R \equiv \sqrt{(\Delta\eta)^2 + (\Delta\phi)^2} = 0.2$ around the lepton, excluding the lepton itself, be less than 15% of the lepton p_T. For the calorimeter, the $\sum E_\text{T}$ deposited inside a cone of $\Delta R = 0.2$ around the lepton, excluding the lepton itself and corrected for contributions from pile-up and, in the case of electrons, shower leakage, is required to be less than 30% of the muon E_T (15% for SA muons) and 20% of the electron E_T.

At the closest approach to the primary vertex, the ratio of the transverse impact parameter d_0 to its uncertainty (d_0 significance) must be smaller than 3.5 (6.5) for muons (electrons) to further reject leptons from heavy flavour decays. The looser electron requirement accounts for the tails in the electron impact parameter distribution due to bremsstrahlung in the ID. The longitudinal impact parameter, $|z_0|$, must be less than 10 mm for both electrons and muons (no requirement is applied on SA muons).

Selection of lepton quadruplets is done separately in each channel: $4\mu, 2e2\mu, 4e$, keeping only a single quadruplet per channel. The inclusion of final-state radiation to charged leptons has followed the same approach described in Ref. [33]. Candidate quadruplets are formed by selecting two opposite-sign, same-flavour lepton pairs ($\ell^+\ell^-$). The two leading-p_T leptons of the quadruplet must have $p_T > 20$ and 15 GeV, respectively, while the third lepton must have $p_T > 10$ (8) GeV if it is an electron (muon). The four leptons of a quadruplet are required to be separated from each other by $\Delta R > 0.1$ (0.2) for same (different) flavour. Only events where the selected leptons fire the triggers used in this analysis are accepted. At most one SA or a CaloTag muon is allowed in each quadruplet.

For each channel, the lepton pair with the mass closest to the Z boson mass is selected as the leading dilepton pair and its invariant mass, m_{12}, is required to be between 50 and 120 GeV, while, due to kinematic cuts in the generated signal samples, its transverse momentum should be above 2 GeV. The sub-leading $\ell^+\ell^-$ pair with the largest invariant mass, m_{34}, among the remaining possible pairs, is selected in the invariant mass range $12 < m_{34} < 120$ GeV.

In the $4e$ and 4μ channels all possible $\ell^+\ell^-$ pairs are required to have $m_{\ell^+\ell^-} > 5$ GeV, to reject events containing $J/\psi \to \ell^+\ell^-$ decays.

There is no jet requirement for 4ℓ event selection, and all the selected 4ℓ events must lie in the $80 < m_{4\ell} < 1000$ GeV range.

5 Background Estimation

The dominant reducible sources of background for this analysis are from Z + jets and $t\bar{t}$ processes and are estimated from data. Contributions from ZW, $Z\gamma$, tZ as well as from the irreducible backgrounds from $t\bar{t}Z$, VVV, ZH and double-DY processes are estimated from simulation.

The reducible background is estimated separately for the two different final states: $\ell\ell + \mu\mu$ and $\ell\ell + ee$, where $\ell\ell$ ($\ell = e, \mu$) is the leading lepton pair. The $\ell\ell + \mu\mu$ background arises from Z + jets and $t\bar{t}$ processes where the Z + jets contribution involves the associated production of a Z boson and heavy flavoured hadrons, which decay semi-leptonically, and a component arising from Z + light-flavour jets with subsequent π/K in-flight decays.

The background for $\ell\ell + ee$ final states arises from jets misidentified as electrons, which can be light-flavour hadrons misidentified as electrons, photon conversions reconstructed as electrons and non-isolated electrons from heavy-flavour hadronic decays.

For both the $\ell\ell + \mu\mu$ and the $\ell\ell + ee$ cases, the number of background events is estimated from a fit performed simultaneously to three orthogonal control regions, each of them providing information on one or more background components. The fit is based on the mass of the leading dilepton, m_{12}, which peaks at the Z mass for the Z + jets component and has a broad distribution for the $t\bar{t}$ component. The three control regions are fit simultaneously to extract the different components of the reducible background, using a profile likelihood approach where the input template shapes for Z + jets and $t\bar{t}$ are obtained from simulation. The fitted yields in the control regions are extrapolated to the signal region using efficiencies, referred to as transfer factors, obtained from simulation.

$\ell\ell + \mu\mu$ background control regions. The three control regions are defined based on the impact parameter significance and isolation variables of the sub-leading muon pair and are constructed as follows:

- A heavy flavour enriched control region where at least one of the muons in the second pair fails the impact parameter significance requirement while the isolation requirement is relaxed;
- A light flavour enriched control region where at least one of the muons in the second pair fails the isolation requirement but passes the impact parameter significance cut;
- A $t\bar{t}$ enriched region where the leading lepton pair is made of opposite sign and different flavour leptons while for the muons of the second pair there is no charge requirement, the isolation cut is relaxed and the muons fail the impact parameter requirement.

A fourth $\ell\ell\mu\mu$ region is populated by both Z + jets and $t\bar{t}$. The leading lepton pair is required to fulfill the full selection criteria, while there is neither isolation nor impact parameter requirements on the sub-leading muon pair. This region is used as the validation region to check the fit results and verify the agreement between data and MC.

$\ell\ell + ee$ background control regions. The three control regions are defined based on the impact parameter significance, isolation and electron identification requirements on the second electron pair. In all control regions at least one of the electrons in the second pair is required to fail the identification criteria. These regions are constructed as follows:

- A Z + jets enriched control region where at least one of the electrons of the second pair fails the track isolation and no calorimeter isolation is required;
- An additional Z + jets enriched control region where no charge requirement is made on the electrons of the second pair, while at least one of these electrons fails the impact parameter selection and no calorimeter or track isolation is required;
- A $t\bar{t}$ enriched region, where the leading lepton pair is selected from opposite sign and different flavour leptons while there is no charge requirement for the sub-leading electron pair. At least one of the electrons of the second pair fails the calorimeter isolation requirement and neither track isolation nor impact parameter requirements are applied.

A validation region for the $\ell\ell ee$ channel is defined by dropping the calorimeter isolation and requesting that at least one electron in the sub-leading pair fails the electron identification. Each candidate in the pair is required to pass the impact parameter and the track isolation selections. Similarly to the $\ell\ell + \mu\mu$ case, this region is used to check the fit outcome and verify the resulting agreement between data and MC.

The residual contributions from ZZ and ZW production in all control regions are estimated from simulation. The purity of the Z + jets and $t\bar{t}$ backgrounds in the control regions is above 95%.

In the validation regions, the post-fit MC predictions agree with the data within the statistical uncertainty.

The background estimations from data and MC are shown in Table 1.

The major uncertainties for the fitted reducible background come from the control sample statistics followed by the systematic uncertainty in the transfer factors. The latter is evaluated from the difference in the selection efficiency determined in data and simulation in dedicated control regions using leptons accompanying $Z \to \ell^+\ell^-$ candidates, where the leptons composing the Z boson candidate are required to satisfy isolation and impact parameter criteria. Events with four leptons are excluded. For the MC estimated background the systematic uncertainties mainly come from theoretical cross section uncertainties for different processes and from luminosity uncertainties in normalisations. The differential distributions for all background processes are taken from simulation.

The background estimation has been cross-checked with an alternative method, described in Ref. [3, 34], called fake-factor method. The results from this cross-check are found to be consistent within uncertainties with those described above.

Table 1: Number of background events expected per channel.

Process	$4e$	4μ	$2e2\mu$
$t\bar{t}$	0.45 ± 0.24	0.68 ± 0.19	1.3 ± 0.5
Z + jets	0.6 ± 0.29	5.3 ± 1.5	6.3 ± 1.4
Diboson	1.25 ± 0.18	0.83 ± 0.18	2.84 ± 0.34
Triboson	0.67 ± 0.12	0.97 ± 0.14	1.46 ± 0.19
Z+top	0.62 ± 0.15	1.19 ± 0.32	1.7 ± 0.5

6 Cross section extraction method

Two cross sections are extracted from the number of observed events. One is the fiducial cross section, σ_{4l}^{fid}, in the experimental phase space defined by the event selection criteria and the other is the cross section, σ_{4l}^{ext}, in an extended common phase space where electrons and muons have the same geometric and kinematic acceptance. The fiducial phase space is defined in Table 2. The extended phase space for the 4ℓ cross-section extraction is defined by $80 < m_{4\ell} < 1000$ GeV, $m_{\ell^+\ell^-} > 4$ GeV, $p_T^{Z_{1,2}} > 2$ GeV, 4 leptons each with $p_T > 5$ GeV and $|\eta| < 2.8$.

The cross section measurement is performed using a likelihood fit described below. For a given channel i, the observed number of events, N^i_{obs}, follows a Poisson distribution, $\text{Pois}(N^i_{\text{obs}}, N^i_{\text{pred}})$, the mean of which, $N^i_{\text{pred}} = N^i_s + N^i_b$, is the sum of the expectations for signal and background yields. These yields depend on the fiducial cross section and the nuisance parameters, $\vec{x}$, which represent the experimental and theoretical uncertainties as the following:

$$N^i_s(\sigma^{\text{fid}}_{4l}, \vec{x}) = N^i_s(\sigma^{\text{fid}}_{4l}, 0)(1 + \sum_k x_k S^i_k), \tag{1}$$

$$N^i_b(\vec{x}) = N^i_b(0)(1 + \sum_k x_k B^i_k), \tag{2}$$

where S^i_k and B^i_k are the relative systematic effects on the signal and background, respectively, due to the k-th source of systematic uncertainty. The central expectation of the signal yield, corresponding to the systematic sources at the nominal value (referred to as the nuisance-free expectation), is given by :

$$N^i_s(\sigma^{\text{fid}}_{4l}, 0) = \mathcal{L} \cdot C_{4\ell} \cdot K_\tau \cdot \sigma^{\text{fid}}_{4l} \tag{3}$$

where $\mathcal{L}$ is the integrated luminosity, and $C_{4\ell}$ is the ratio of the number of accepted signal events to the number of generated events in the fiducial phase space. Corrections are applied to $C_{4\ell}$ to account for measured differences in trigger and reconstruction efficiencies between simulated and data samples and for the extrapolation to the fiducial phase space. The $C_{4\ell}$ values are 53.3%, 82.2% and 67.7% for $4e$, 4μ, and $2e2\mu$ channels, respectively. The contribution from τ-lepton decays is removed by a correction term $K_\tau = 1 + \frac{N^{\text{MC}}_\tau}{N^{\text{MC}}_{\text{sig}}}$, where N^{MC}_τ is the number of accepted simulated 4ℓ events in which at least one of the Z bosons decays into τ-lepton pairs, and $N^{\text{MC}}_{\text{sig}}$ is the number of accepted simulated ZZ events with decays into electrons or muons.

Cross-section measurements are extracted for a single channel or any combination of channels, using a likelihood method. The likelihood function is:

$$L(\sigma^{\text{fid}}_{4l}, \vec{x}) = \prod_i \text{Pois}(N^i_{\text{obs}}, N^i_{\text{pred}}(\sigma^{\text{fid}}_{4l}, \vec{x})) \cdot e^{-\frac{\vec{x}^2}{2}} \tag{4}$$

Table 2: List of selection cuts which define the fiducial region of the cross section measurement. Same flavour opposite sign lepton pairs are denoted as SFOS, the leading lepton pair mass as m_{12}, and the sub-leading lepton pair mass as m_{34}. The four-momenta of all final state photons within $\Delta R = 0.1$ of a lepton are added to the four-momentum of that lepton.

Lepton selection	
Muons:	$p_{\mathrm{T}} > 6$ GeV, $\lvert\eta\rvert < 2.7$
Electrons:	$p_{\mathrm{T}} > 7$ GeV, $\lvert\eta\rvert < 2.5$
Lepton pairing	
Leading pair:	SFOS lepton pair with smallest $\lvert m_Z - m_{\ell\ell}\rvert$
Subleading pair:	The remaining SFOS with the largest $m_{\ell\ell}$
For both pairs:	$p_T^{\ell^+\ell^-} > 2$ GeV
Event selection	
Lepton $p_T^{\ell_1,\ell_2,\ell_3}$:	$> 20, 15, 10(8\ if\ \mu)$ GeV
Mass requirements:	$50 < m_{12} < 120$ GeV
	$12 < m_{34} < 120$ GeV
Lepton separation:	$\Delta R(\ell_i, \ell_j) > 0.1$ (0.2) for same- (different-) flavour leptons
J/ψ veto:	$m(\ell_i^+, \ell_j^-) > 5$ GeV
4ℓ mass range:	$80 < m_{4\ell} < 1000$ GeV

where the product runs over the channels to be considered.

For the extended phase space the likelihood function is parametrized as a function of the extended cross section similar to the one shown in the equation 3. and multiplied by the fiducial acceptance $A_{4\ell}$, which is the ratio of the number of events within the fiducial phase space region to the total number of generated events in the extended phase space. The fiducial acceptance $A_{4\ell}$ are evaluated using simulation to be 41.6%, 50.3%, 42.2%, for $4e$, 4μ, and $2e2\mu$ channels, respectively. The differences are due to the electron and muon geometric detection coverage.

To find the central value of cross section σ, the likelihood function is maximized simultaneously for the nuisance parameters and σ. Correlations between the signal and background systematic uncertainties are taken into account in the likelihood fitting procedure.

7 Systematic Uncertainties

Systematic uncertainties on the measurement arise from uncertainties on the integrated luminosity, the experimental calibrations of the energy and momentum, and the lepton detection efficiencies, as well as the theoretical modelling of signal acceptance, and the background estimation.

The overall uncertainty in the integrated luminosity is ±2.8% as described in Ref. [35].

A summary of the uncertainties in $C_{4\ell}$, $A_{4\ell}$, and $A_{4\ell} \times C_{4\ell}$ is given in Tables 3 and 4.

The effect on the expected signal event yields due to experimental systematic uncertainties is determined from the uncertainties on lepton energy and momentum scales and resolutions, as well as the uncertainties on efficiencies of the lepton reconstruction and identification. The major uncertainties come from the uncertainties on lepton reconstruction and identification efficiencies [36–38].

The uncertainties on the signal acceptance for both $C_{4\ell}$ and $A_{4\ell}$ include theoretical uncertainties from the choice of QCD scales and PDF set. The scales are varied independently from 0.5 to 2.0 times the nominal values of μ_{R} and μ_{F}. The PDFs uncertainties are estimated by using the envelope [39] of variations of different PDF sets, CT10, MSTW2008 [40] and NNPDF2.3 [41].

The $C_{4\ell}$ uncertainty is mostly experimental and of order of 2-5%, while the $A_{4\ell}$ uncertainty is entirely theoretical and of order of 3-5%. The relative uncertainties on the $C_{4\ell}$ factors are 4.9%, 1.9%, and 2.5% for $4e$, 4μ, and $2e2\mu$, respectively. The uncertainties on $C_{4\ell}$ due to higher-order corrections to the gg production processes are less than 0.6%. This is estimated by applying an approximate NNLO K-factor determined for the Higgs-boson production, assuming that it is applicable to the normalization of the continuum $gg \to ZZ$ production cross section.

Uncertainties on the $C_{4\ell}$, as a function of $m_{4\ell}$ and $p_T^{4\ell}$, are also computed for the differential cross section measurements. In the low mass region ($m_{4\ell} < 150$ GeV), the relative uncertainties on $C_{4\ell}$ vary from 4-9%, 1.7-2.7%, and 2-5% for $4e$, 4μ, and $2e2\mu$ channel, respectively. In the mass region $m_{4\ell} > 150$ GeV, they are mostly flat as a function of $m_{4\ell}$ and are about 4%, 1.8%, and 3% for $4e$, 4μ, and $2e2\mu$ channel, respectively.

The relative uncertainties on the $A_{4\ell}$ are 1.2%, 1.0%, and 1.6% for $4e$, 4μ, and $2e2\mu$ channel, respectively, evaluated by comparing POWHEG-BOX and MCFM MC samples with the same approach for the QCD scales and the PDF uncertainties as described earlier. The QCD scale uncertainties do not change when going from NLO to NNLO for the signal normalisation for the $q\bar{q} \to 4\ell$ events [18]. An additional uncertainty (3-4%) is included in the $A_{4\ell}$ uncertainty estimate to account for the uncertainty of the Higgs boson NNLO K-factor normalisation correction of the non-resonant 4ℓ signal from gluon fusion (labelled "extra gg corrections" in Tables 3 and 4).

The largest source of systematic uncertainty on the cross section in the extended phase space is the theoretical uncertainty on the K-factors (4.6%) followed by the electron identification (4.1%).

Table 3: The combined uncertainties on the efficiency correction factor $C_{4\ell}$, evaluated by the quadratic sum of the uncertainties from different sources, including electron and muon identification and theoretical uncertainties due to PDFs, QCD scales, and parton shower modelling. Extra uncertainties due to higher-order corrections for the gg process (NNLO K-factors for Higgs boson production applied to the inclusive gg process) are also given.

Sources	$\Delta C_{4\ell}/C_{4\ell}$		
	$4e$	4μ	$2e2\mu$
Experimental (e)	4.8%	-	2.3%
Experimental (μ)	-	1.8%	0.9%
Theoretical	0.1%	0.1%	0.2%
Extra gg corrections	0.6%	0.2%	0.3%
Combined uncertainty	4.9%	1.9%	2.5%

Table 4: Theoretical uncertainties on $A_{4\ell}$ and $A_{4\ell} \times C_{4\ell}$ due to PDFs, QCD scales and parton shower modelling. Extra uncertainties due to higher-order corrections for the gg process (NNLO K-factors for Higgs boson production applied to the inclusive gg process) are also given.

Sources	$4e$	4μ	$2e2\mu$
	$\Delta A_{4\ell}/A_{4\ell}$		
Theoretical	1.2%	1.0%	1.6%
Extra gg corrections	4.0%	3.0%	3.9%
	$\Delta(A_{4\ell} \times C_{4\ell})/(A_{4\ell} \times C_{4\ell})$		
Theoretical	1.4%	1.1%	1.7%
Extra gg corrections	4.6%	3.2%	4.2%

Table 5: Summary of the observed and predicted number of 4ℓ events in different 4ℓ channels. N^{Data} denotes the selected number of data candidates. $N^{Total}_{expected}$ denotes the total predicted number of events (including τ contributions) for signal plus background. N^{signal}_{non-gg} and the N^{signal}_{gg} denote the predicted non-gg signal and the gg signal (no NNLO K-factor has been applied), respectively. N^{MC}_{τ} denotes the number of τ contributions. N_{bkg} denotes the total estimated number of background events (from data and MC). The listed uncertainties include statistical and experimental systematic uncertainties. The theoretical uncertainties are not included.

Channel	N^{Data}	$N^{Total}_{expected}$	N^{signal}_{non-gg}	N^{signal}_{gg}	N^{MC}_{τ}	N_{bkg}
$4e$	85	80 ± 4	68.4 ± 3.4	6.24 ± 0.31	1.28 ± 0.06	3.6 ± 0.5
4μ	156	150.2 ± 2.9	128.2 ± 2.5	11.00 ± 0.21	2.18 ± 0.09	9.0 ± 1.5
$2e2\mu$	235	205 ± 5	172 ± 5	16.0 ± 0.4	3.08 ± 0.13	13.6 ± 2.1
Total	476	435 ± 9	369 ± 9	33.3 ± 0.8	6.54 ± 0.14	26.2 ± 3.6

The overall uncertainty on the background estimation is 12%. The contributions from different sources and channels are already given in Table 1.

8 Results

8.1 Cross-section Measurements

The numbers of expected and observed events after applying all selection criteria are shown in Table 5. A total of 476 candidate events is observed with a background expectation of 26.2 ± 3.6 events. The observed and predicted $m_{4\ell}$ and p_T^{4l} distributions for the selected events are shown in Figure 4.

The measured cross sections in the fiducial and extended phase space for different 4ℓ channels and their combinations are summarised in Tables 6 and 7 respectively, and compared to the SM predicted cross sections. One should note that the cross section for non-resonant ZZ production from the gg-induced signal is only calculated at LO approximation, which could be significantly under estimated.

Table 6: Measured fiducial cross sections σ^{fid}_{4e}, $\sigma^{fid}_{4\mu}$, and $\sigma^{fid}_{2e2\mu}$, compared to their SM prediction. One should note that the non-resonant gg-induced signal cross section is only calculated at LO approximation.

	Fiducial Cross Section [fb]	SM Prediction [fb]
σ^{fid}_{4e}	$7.4^{+0.9}_{-0.8}$ (stat.) $^{+0.4}_{-0.3}$ (syst.) $^{+0.2}_{-0.2}$ (lumi.)	6.9 ± 0.6
$\sigma^{fid}_{4\mu}$	$8.7^{+0.8}_{-0.7}$ (stat.) $^{+0.2}_{-0.2}$ (syst.) $^{+0.3}_{-0.2}$ (lumi.)	8.3 ± 0.7
$\sigma^{fid}_{2e2\mu}$	$15.9^{+1.1}_{-1.1}$ (stat.) $^{+0.5}_{-0.4}$ (syst.) $^{+0.5}_{-0.4}$ (lumi.)	13.7 ± 1.2

Table 7: Measured cross sections in the extended phase space, σ^{ext}_{4e}, $\sigma^{ext}_{4\mu}$, $\sigma^{ext}_{2e2\mu}$, and their combinations, compared to their SM prediction. One should note that the non-resonant gg-induced signal cross section is only calculated at LO approximation.

	Cross Section in the extended phase space [fb]	SM Prediction [fb]
σ^{ext}_{4e}	$17.8^{+2.1}_{-2.0}$ (stat.) $^{+1.5}_{-1.1}$ (syst.) $^{+0.5}_{-0.5}$ (lumi.)	16.4 ± 1.4
$\sigma^{ext}_{4\mu}$	$17.3^{+1.5}_{-1.4}$ (stat.) $^{+0.9}_{-0.7}$ (syst.) $^{+0.5}_{-0.5}$ (lumi.)	16.4 ± 1.4
Combined $\sigma^{ext}_{4e+4\mu}$	$35.0^{+2.4}_{-2.3}$ (stat.) $^{+1.9}_{-1.5}$ (syst.) $^{+1.1}_{-1.0}$ (lumi.)	32.9 ± 1.9
$\sigma^{ext}_{2e2\mu}$	$37.7^{+2.7}_{-2.6}$ (stat.) $^{+2.5}_{-2.0}$ (syst.) $^{+1.1}_{-1.1}$ (lumi.)	32.1 ± 2.0
Combined $\sigma^{ext}_{4\ell}$	73^{+4}_{-4} (stat.) $^{+4}_{-4}$ (syst.) $^{+2}_{-2}$ (lumi.)	65 ± 4

8.2 Differential Cross-Section Measurement

The measurement of the differential cross section is performed in the fiducial phase space defined in Table 2. The events from all the three 4ℓ channels are combined into a common sample for the unfolding procedure explained below. The unfolding is done as a function of the two kinematic variables $m_{4\ell}$ and $p_T^{4\ell}$. The $m_{4\ell}$ spectrum is essential for the study of the different production mechanisms, while the $p_T^{4\ell}$ spectrum is sensitive to the higher-order QCD corrections and to QCD resummation effects at small $p_T^{4\ell}$ [12]. The high $p_T^{4\ell}$ region is sensitive to top-loop effects in $gg \to H$ production as well as to anomalous triple-boson couplings.

The measured distributions can be corrected for detector effects, namely resolution, acceptance and efficiency, through the process of unfolding. The unfolding procedure converts the measured distributions into particle-level distributions enabling comparisons with theoretical predictions.

The iterative Bayesian unfolding proposed in Ref. [42] is applied here. In the unfolding of binned data, the effects of the experimental acceptance and resolution are expressed in terms of a response matrix, where each element corresponds to the probability of an event in the i-th truth bin being reconstructed in the j-th measured bin. The response matrix is combined with the measured spectrum to form a likelihood, which is then multiplied by a prior distribution to produce the posterior probability of the true spectrum. The SM prediction is used as the initial prior, and once the posterior probability is obtained, it is used as the prior for the next iteration after smoothing. The spectrum becomes insensitive to the initial prior after a few iterations. The differences between successive iterations can be used to estimate the stability of the unfolding method. In this analysis four iterations have been performed.

The unfolded distributions are shown in Figure 5, where the differential cross section is presented as a function of $m_{4\ell}$ and $p_T^{4\ell}$ and compared to theory predictions. The black points shown in the figures are the measurements with combined statistical and systematic uncertainties. The theoretical predictions are the sum of the differential cross sections of the $q\bar{q} \to 4\ell$ and $gg \to 4\ell$ processes. The LO cross sections are used for the non-resonant gg-induced signals. The cross sections of the on-shell Higgs boson are normalized to include the NNLO QCD and NLO EW effects as summarized in Ref. [21]. The $q\bar{q}$ productions are corrected with the NNLO QCD and the NLO EW K-factors for the $m_{4\ell}$ spectrum for $m_{4\ell} > 2 \times m_Z$. For the $p_T^{4\ell}$ spectrum, the $q\bar{q}$ signal prediction is calculated by POWHEG-BOX at NLO QCD.

The uncertainties on the differential cross section measurements are dominated by the statistical uncertainties of the data in each bin. For example, in the $m_{4\ell}$ regions between the Z- and the H-peak and between the Higgs-boson mass m_H and $m_{4\ell} < 180$ GeV, the statistical uncertainties are of the order of 45% and 20%, respectively. In the high mass region ($m_{4\ell} > 180$ GeV) they are of the order of 10%. Furthermore, one should note that the NNLO QCD corrections are missing for the $q\bar{q} \to 4\ell$ production calculation for the mass region $m_{4\ell} < 2 \times m_Z$.

In the $m_{4\ell}$ bin of 120-130 GeV, which is dominated by the resonant Higgs-boson contribution, the ratio of data over MC prediction is compatible with the ATLAS measurement [33] of the Higgs-boson signal strength of $\mu_H = 1.44^{+0.40}_{-0.33}$. The data points in the $m_{4\ell}$ spectrum between 140 to 180 GeV are slightly more than 1σ above the theoretical predictions, which could be due to the missing higher-order correction just noted. Some discrepancy is also observed in the lowest bin and in the region between 30 - 50 GeV of the $p_T^{4\ell}$ spectrum.

8.3 Extraction of the gg Signal Contribution in the $m_{4\ell} > 180$ GeV Region

The extraction of the signal strength of the non-resonant $gg \to 4\ell$ production is performed in the high mass region, $m_{4\ell} > 180$ GeV, where this production mode is dominated by the continuum $gg \to ZZ$ through a quark-box diagram intermediate state. Additional contributions come from the off-shell Higgs-boson production and the interference between Higgs boson and continuum ZZ.

The $m_{4\ell}$ variable is chosen as the discriminant to extract the gg signal strength with respect to the LO gg prediction: $\mu_{gg} = \sigma(data)/\sigma(LO)$.

The contribution of the $q\bar{q} \to ZZ$ production is constraint to the best theory knowledge (which accounts for QCD NNLO and EW NLO m_{4l}-dependent corrections) and μ_{gg} is extracted from a likelihood fit using the reconstructed $m_{4\ell}$ distributions. The likelihood function is built similar to the method employed for measuring the integrated cross sections (Section 6). The experimental uncertainties are treated as fully correlated between $q\bar{q}$ and gg processes. The theoretical uncertainties, including the uncertainties on the normalisation of the $q\bar{q} \to ZZ \to 4\ell$, the shapes of 4ℓ spectra from both the $q\bar{q}$ and gg initial states, and the acceptance described in Section 7, are taken into account. The $m_{4\ell}$ distribution of the data, the fit, the expectation from non-gg signal processes and the background are shown in Figure 6 for comparison. The fit result is

$$\mu_{gg} = 2.4 \pm 1.0(stat.) \pm 0.5(syst.) \pm 0.8(theory),$$

which corresponds to a gg-induced cross section of 3.1 fb with the same relative uncertainties as μ_{gg} itself in the inclusive fiducial volume as defined in Table 2 with the additional requirement of $m_{4\ell} > 180$ GeV. The largest uncertainty is statistical. The theoretical uncertainty is also sizable due to normalisation uncertainty of the $q\bar{q} \to ZZ$ process.

The theoretical estimation of $m_{4\ell}$-dependent K-factor for off-shell Higgs-boson production given in Ref. [2] is approximately 2.7-3.1 (with CT10NNLO PDF) and that given in Ref. [24] for the interference term are 2.05-2.45. These are compatible with the result obtained by this analysis, where the gg-induced events are predominantly from the continuum ZZ production mechanism. Applying the higher-order corrections to both the cross section of the off-shell Higgs-boson production and the contribution of the interference term, while keeping the LO cross section for the continuum $gg \to ZZ$, the relative change of the μ_{gg} fit result is negligible (approximatively 0.35%).

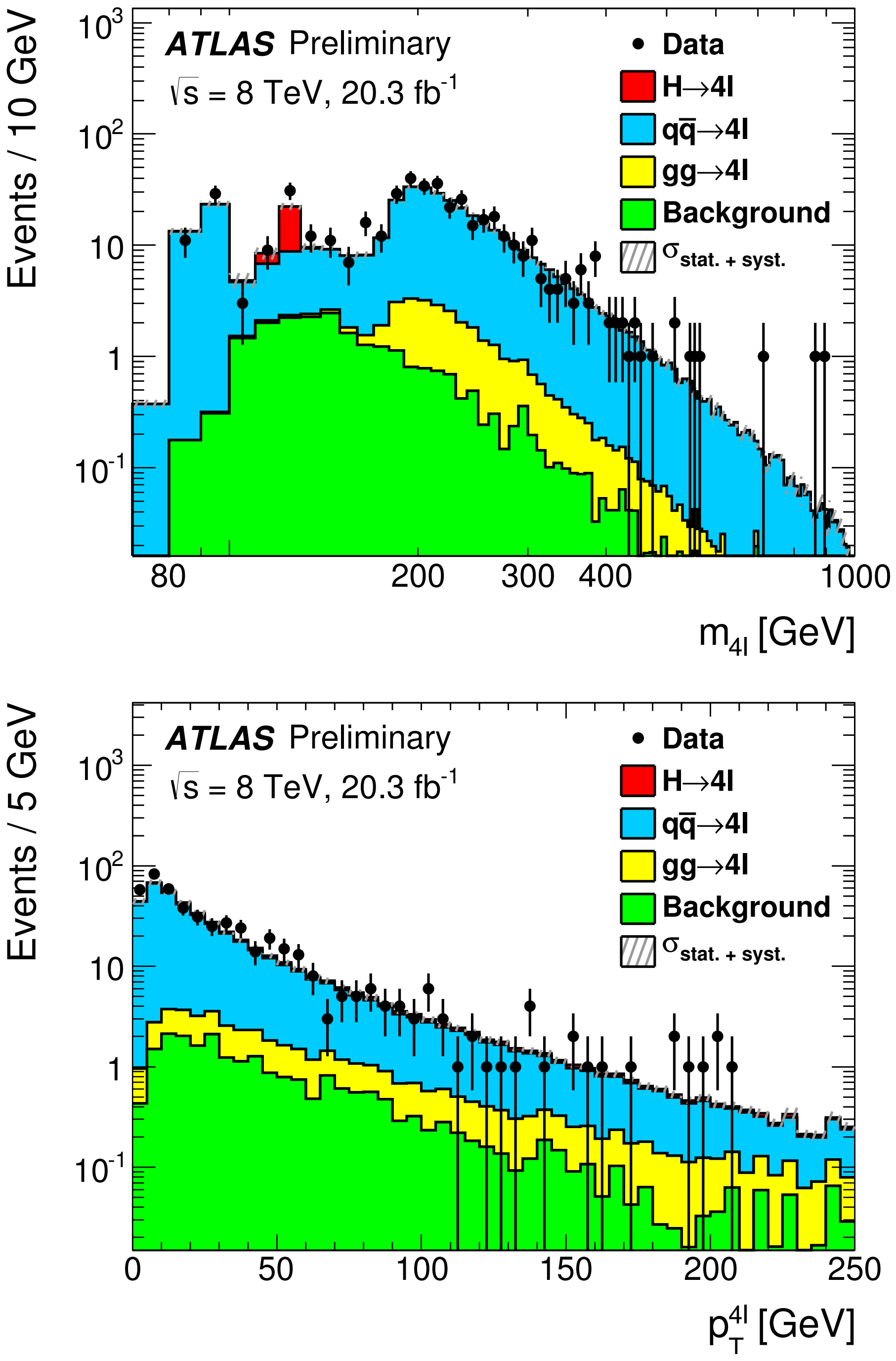

Figure 4: Data and MC prediction comparison for selected events as a function of the invariant mass $m_{4\ell}$ (top) and the transverse momentum p_T^{4l} (bottom) of the four-lepton system. The solid colours show the expected contributions from signal and background and the black points represent data with statistical error bars.

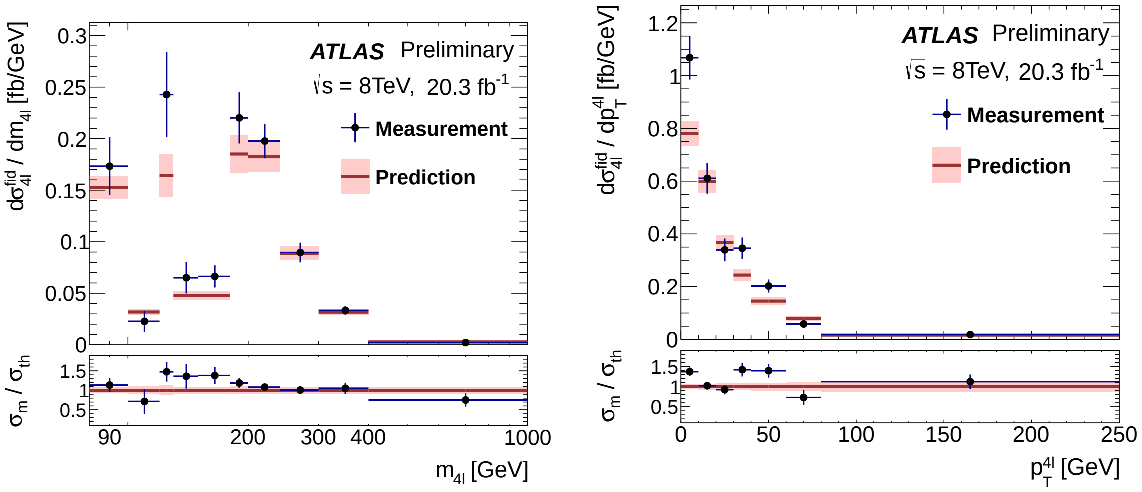

Figure 5: The measured differential cross-section distributions (the black points) of $m_{4\ell}$ (left) and $p_T^{4\ell}$ (right), unfolded into the fiducial volume, and compared to theory predictions (red histogram). The combined statistical and systematic uncertainties of the measurements are shown as the error-bars of the unfolded spectra. The theoretical predictions are the sum of the differential cross sections of the $q\bar{q} \rightarrow 4\ell$ and $gg \rightarrow 4\ell$ processes, where the LO cross sections are used for the non-resonant gg-induced signals, and the cross sections of the on-shell Higgs boson and the $q\bar{q}$ productions are corrected with the NNLO K-factors for the $m_{4\ell}$ spectrum; but for $p_T^{4\ell}$, the NLO and LO predictions are used for the $q\bar{q}$ and the gg process, respectively. The total theoretical uncertainties are shown as error bands evaluated by the quadratic sum of the contributions from parton showers, QCD scales, PDF sets, and electroweak corrections.

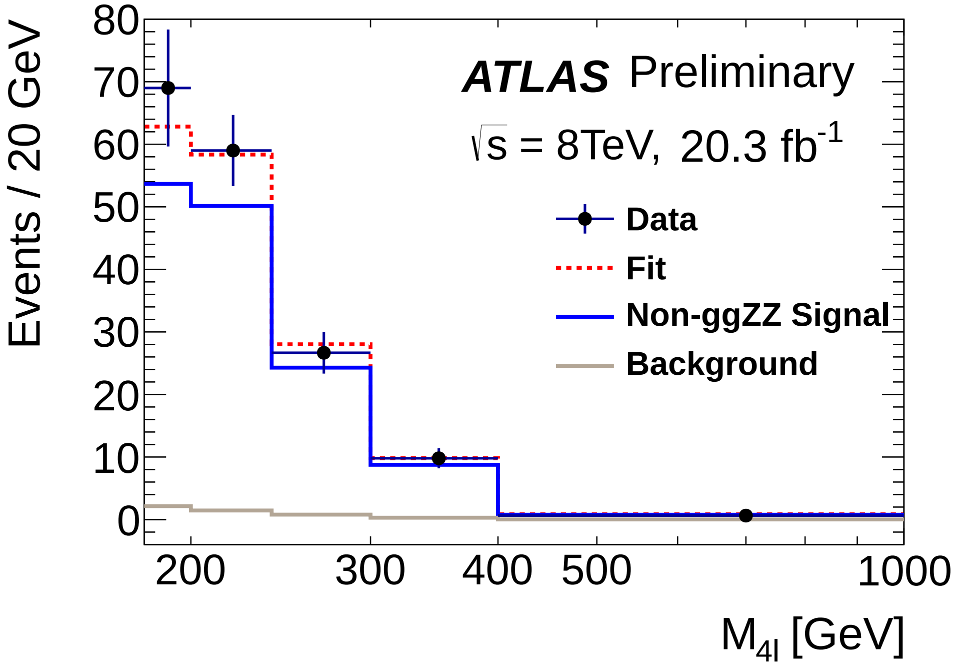

Figure 6: Comparison of the $m_{4\ell}$ spectra between the data (black points with error-bars) and the prediction (red histogram) after the likelihood fit of μ_{gg}. The non-gg signal from the theoretical prediction (blue histogram) and the background (brown histogram) are also shown. The gg contribution is the difference between data and the sum of the non-gg signal and the background.

9 Summary and Conclusion

The measurement of four-lepton production in proton-proton collisions at $\sqrt{s} = 8$ TeV is presented using data corresponding to an integrated luminosity of 20.3 fb^{-1} collected with the ATLAS detector at the LHC. In total, 476 4ℓ candidate events are observed, with a background expectation of 26.2 ± 3.6 events, in the four-lepton invariant mass range between 80 and 1000 GeV. The 4ℓ production cross sections are determined in both fiducial and extended phase spaces. The measured cross section in the extended phase space, defined by $80 < m_{4\ell} < 1000$ GeV, $m_{\ell^+\ell^-} > 4$ GeV, $p_T^{Z_{1,2}} > 2$ GeV, 4 leptons each with $p_T > 5$ GeV and $|\eta| < 2.8$, is found to be 73 ± 4 (stat.) ± 4 (syst.) ± 2 (lumi.) fb, and is compared to a SM prediction of 65 ± 4 fb. The first measurements at the LHC of the 4ℓ differential cross sections are performed by unfolding the $m_{4\ell}$ and the $p_T^{4\ell}$ spectra. In the mass range above 180 GeV, assuming the theoretical constraint on the $q\bar{q}$ production cross section calculated with perturbative NNLO QCD and NLO Electroweak corrections, the signal strength of the gluon-fusion component with respect to the LO prediction is determined to be $\mu_{gg} = 2.4 \pm 1.0(stat.) \pm 0.5(syst.) \pm 0.8(theory)$.

Acknowledgements

We thank CERN for the very successful operation of the LHC, as well as the support staff from our institutions without whom ATLAS could not be operated efficiently.

We acknowledge the support of ANPCyT, Argentina; YerPhI, Armenia; ARC, Australia; BMWFW and FWF, Austria; ANAS, Azerbaijan; SSTC, Belarus; CNPq and FAPESP, Brazil; NSERC, NRC and CFI, Canada; CERN; CONICYT, Chile; CAS, MOST and NSFC, China; COLCIENCIAS, Colombia; MSMT CR, MPO CR and VSC CR, Czech Republic; DNRF, DNSRC and Lundbeck Foundation, Denmark; EPLANET, ERC and NSRF, European Union; IN2P3-CNRS, CEA-DSM/IRFU, France; GNSF, Georgia; BMBF, DFG, HGF, MPG and AvH Foundation, Germany; GSRT and NSRF, Greece; RGC, Hong Kong SAR, China; ISF, MINERVA, GIF, I-CORE and Benoziyo Center, Israel; INFN, Italy; MEXT and JSPS, Japan; CNRST, Morocco; FOM and NWO, Netherlands; BRF and RCN, Norway; MNiSW and NCN, Poland; GRICES and FCT, Portugal; MNE/IFA, Romania; MES of Russia and NRC KI, Russian Federation; JINR; MSTD, Serbia; MSSR, Slovakia; ARRS and MIZŠ, Slovenia; DST/NRF, South Africa; MINECO, Spain; SRC and Wallenberg Foundation, Sweden; SER, SNSF and Cantons of Bern and Geneva, Switzerland; NSC, Taiwan; TAEK, Turkey; STFC, the Royal Society and Leverhulme Trust, United Kingdom; DOE and NSF, United States of America.

The crucial computing support from all WLCG partners is acknowledged gratefully, in particular from CERN and the ATLAS Tier-1 facilities at TRIUMF (Canada), NDGF (Denmark, Norway, Sweden), CC-IN2P3 (France), KIT/GridKA (Germany), INFN-CNAF (Italy), NL-T1 (Netherlands), PIC (Spain), ASGC (Taiwan), RAL (UK) and BNL (USA) and in the Tier-2 facilities worldwide.

References

[1] J. M. Campbell, R. K. Ellis and C. Williams, *Bounding the Higgs width at the LHC using full analytic results for* $gg- > e^-e^+\mu^-\mu^+$, JHEP **1404** (2014) 060, arXiv: `1311.3589 [hep-ph]`.

[2] G. Passarino, *Higgs CAT* (2013), arXiv: `1312.2397 [hep-ph]`.

[3] ATLAS Collaboration, *Measurements of Four-Lepton Production at the Z Resonance in pp Collisions at $\sqrt{s} = 7$ and 8 TeV with ATLAS*, Phys. Rev. Lett. **112,** (2014) 231806, arXiv: `1403.5657 [hep-ex]`.

[4] CMS Collaboration, *Observation of Z decays to four leptons with the CMS detector at the LHC*, J. High Energy PHys. **2012**.12 (2012), arXiv: `1210.3844 [hep-ex]`.

[5] ATLAS Collaboration, *Observation of a new particle in the search for the Standard Model Higgs boson with the ATLAS detector at the LHC*, Physics Letters B **716,** (2012) 1, ISSN: 0370-2693, arXiv: `1207.7214 [hep-ex]`.

[6] CMS Collaboration, *Observation of a new boson at a mass of 125 GeV with the CMS experiment at the LHC*, Physics Letters B **716,** (2012) 30, ISSN: 0370-2693, arXiv: `1207.7235 [hep-ex]`.

[7] N. Kauer and G. Passarino, *Inadequacy of zero-width approximation for a light Higgs boson signal*, JHEP **1208** (2012) 116, arXiv: `1206.4803 [hep-ph]`.

[8] F. Caola and K. Melnikov, *Constraining the Higgs boson width with ZZ production at the LHC*, Phys.Rev. **D88** (2013) 054024, arXiv: `1307.4935 [hep-ph]`.

[9] S. Goria, G. Passarino and D. Rosco, *The Higgs Boson Lineshape*, Nucl.Phys. **B864** (2012) 530–579, arXiv: `1112.5517 [hep-ph]`.

[10] ATLAS Collaboration, *Determination of the off-shell Higgs boson signal strength in the high-mass ZZ and WW final states with the ATLAS detector* (2015), arXiv: `1503.01060 [hep-ex]`.

[11] CMS Collaboration, *Constraints on the Higgs boson width from off-shell production and decay to Z-boson pairs*, Physics Letters B **736,** (2014) 64, ISSN: 1405.3455, arXiv: `1405.3455 [hep-ex]`.

[12] M. Grazzini et al., *Transverse-momentum resummation for vector-boson pair production at NNLL+NNLO* (2015), arXiv: `1507.02565 [hep-ph]`.

[13] ATLAS Collaboration, *The ATLAS experiment at the CERN Large Hadron Collider*, JINST **3,** (2008) S08003.

[14] T. Melia et al., *W+W-, WZ and ZZ production in the POWHEG BOX*, JHEP **1111** (2011) 078, arXiv: `1107.5051 [hep-ph]`.

[15] S. Alioli et al., *A general framework for implementing NLO calculations in shower Monte Carlo programs: the POWHEG BOX*, JHEP **1006** (2010) 043, arXiv: `1002.2581 [hep-ph]`.

[16] P. Nason, *A New method for combining NLO QCD with shower Monte Carlo algorithms*, JHEP **0411** (2004) 040, arXiv: `hep-ph/0409146 [hep-ph]`.

[17] H.-L. Lai et al., *New parton distributions for collider physics*, Phys.Rev. **D82** (2010) 074024, arXiv: `1007.2241 [hep-ph]`.

[18] F. Cascioli et al., *ZZ production at hadron colliders in NNLO QCD*, Phys.Lett. **B735** (2014) 311–313, arXiv: `1405.2219 [hep-ph]`.

[19] A. Bierweiler, T. Kasprzik and J. H. K*ü*hn, *Vector-boson pair production at the LHC to O(α3) accuracy* (2013), arXiv: `1305.5402 [hep-ph]`.

[20] T. Sjostrand, S. Mrenna and P. Skands, *A brief introduction to PYTHIA 8.1*, Comput. Phys. Commun. **178,** (2008) 852, arXiv: `0710.3820 [hep-ph]`.

[21] S Heinemeyer et al., *Handbook of LHC Higgs Cross Sections: 3. Higgs Properties* (2013), ed. by S Heinemeyer, arXiv: `1307.1347 [hep-ph]`.

[22] J. Gao et al., *CT10 next-to-next-to-leading order global analysis of QCD*, Phys.Rev. **D89**.3 (2014) 033009, arXiv: `1302.6246 [hep-ph]`.

[23] J. Alwall et al., *The automated computation of tree-level and next-to-leading order differential cross sections, and their matching to parton shower simulations*, JHEP **1407** (2014) 079, arXiv: `1405.0301 [hep-ph]`.

[24] C. S. Li et al., *Soft gluon resummation in the signal-background interference process of* $gg(\rightarrow h^*) \rightarrow ZZ$ (2015), arXiv: `1504.02388 [hep-ph]`.

[25] T. Sjostrand, S. Mrenna and P. Skands, *PYTHIA 6.4 Physics and Manual*, J. High Energy Phys. () 05 (2006) 026, arXiv: `hep-ph/0603175`.

[26] T. Gleisberg et al., *Event generation with SHERPA 1.1*, JHEP **0902** (2009) 007, arXiv: `0811.4622 [hep-ph]`.

[27] M. L. Mangano et al., *ALPGEN, a generator for hard multiparton processes in hadronic collisions*, JHEP **0307** (2003) 001, arXiv: `hep-ph/0206293 [hep-ph]`.

[28] G. Corcella et al., *HERWIG 6: An Event generator for hadron emission reactions with interfering gluons (including supersymmetric processes)*, JHEP **0101** (2001) 010, arXiv: `hep-ph/0011363 [hep-ph]`.

[29] J. Butterworth, J. R. Forshaw and M. Seymour, *Multiparton interactions in photoproduction at HERA*, Z.Phys. **C72** (1996) 637–646, arXiv: `hep-ph/9601371 [hep-ph]`.

[30] ATLAS Collaboration, *The ATLAS simulation infrastructure*, Eur. Phys. J. C **70,** (2010) 823–874, arXiv: `1005.4568 [physics.ins-det]`.

[31] S. Agostinelli et al., *GEANT4: A Simulation toolkit*, Nucl.Instrum.Meth. **A506** (2003) 250–303.

[32] ATLAS Collaboration, *Electron efficiency measurements with the ATLAS detector using the 2012 LHC proton-proton collision data* (2014), ATLAS-CONF-2014-032.

[33] ATLAS Collaboration, *Measurements of Higgs boson production and couplings in the four-lepton channel in pp collisions at center-of-mass energies of 7 and 8 TeV with the ATLAS detector*, Phys.Rev. **D91**.1 (2015) 012006, arXiv: `1408.5191 [hep-ex]`.

[34] ATLAS Collaboration, *Measurement of ZZ production in pp collisions at* $\sqrt{s} = 7$ *TeV and limits on anomalous ZZZ and ZZ*γ *couplings with the ATLAS detector*, JHEP **1303** (2013) 128, arXiv: `1211.6096 [hep-ex]`.

[35] The Luminosity Group, ATL-COM-LUM-2012-013, 2012.

[36] ATLAS Collaboration, *Measurement of the muon reconstruction performance of the ATLAS detector using 2011 and 2012 LHC proton–proton collision data*, Eur. Phys. J. **C74**.11 (2014) 3130, arXiv: `1407.3935 [hep-ex]`.

[37] ATLAS Collaboration,
Electron and photon energy calibration with the ATLAS detector using LHC Run 1 data,
Eur. Phys. J. **C74**.10 (2014) 3071, arXiv: `1407.5063 [hep-ex]`.

[38] ATLAS Collaboration, *Electron reconstruction and identification efficiency measurements with the ATLAS detector using the 2011 LHC proton-proton collision data*,
Eur. Phys. J. **C74**.7 (2014) 2941, arXiv: `1404.2240 [hep-ex]`.

[39] M. Botje et al., *The PDF4LHC Working Group Interim Recommendations* (2011),
arXiv: `1101.0538 [hep-ph]`.

[40] A. Martin et al., *Parton distributions for the LHC*, Eur.Phys.J. **C63** (2009) 189–285,
arXiv: `0901.0002 [hep-ph]`.

[41] R. D. Ball et al., *Parton distributions with LHC data*, Nucl.Phys. **B867** (2013) 244–289,
arXiv: `1207.1303 [hep-ph]`.

[42] G. D'Agostini, *Improved iterative Bayesian unfolding* (2010),
arXiv: `1010.0632 [physics.data-an]`.

Appendix

Following are additional plots pertaining to this analysis.

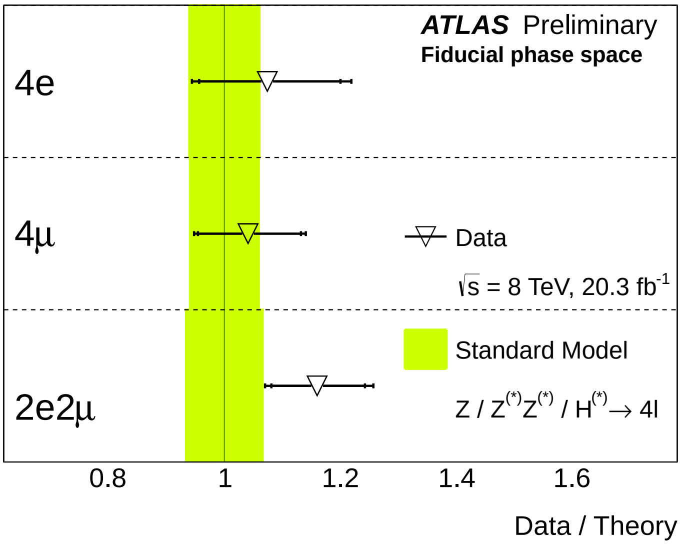

(a)

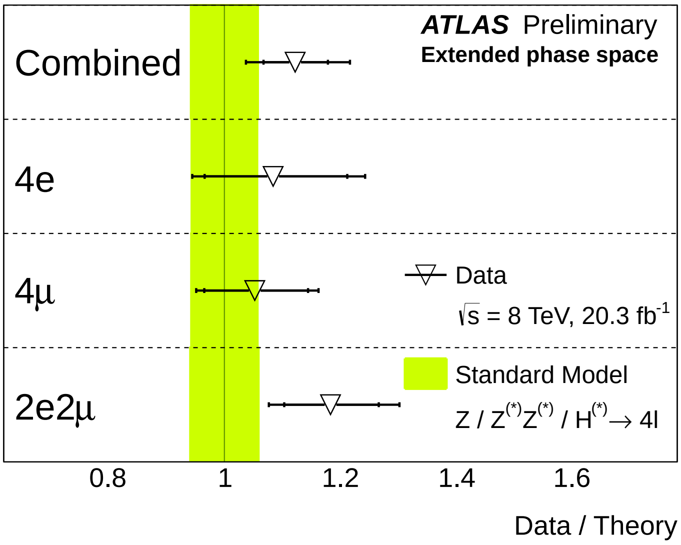

(b)

Figure 7: Expected inclusive cross sections in fiducial and extended phase space divided by the measurements. The results per channel and for the three-channel combinations in the extended phase space, where the assumption that the corresponding channel cross sections are equal, are also presented.

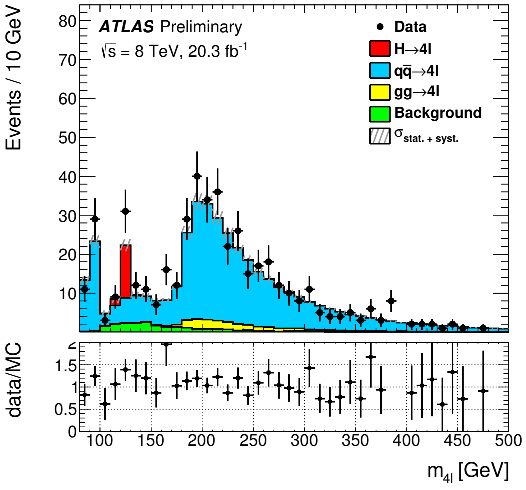

(a)

Figure 8: Invariant mass distribution of the four-lepton system from data (black points with error bars) and expectations from different 4ℓ signal production processes plus the estimated background contributions (solid colour histograms). Events are selected with full 4ℓ event selection criteria. The expectations of the on-shell Higgs boson (from ggF and VBF processes) and the continuum $q\bar{q} \to ZZ$ productions are modelled with POWHEG-BOX and normalisations are corrected with NNLO QCD and NLO EW as a function of $m_{4\ell}$. The prediction of the non-resonant $gg \to ZZ$ production is calculated with MCFM at the LO. Small contributions from the VBF off-shell Higgs boson and continuum ZZ (modelled by MADGRAPH) and from VH and $t\bar{t}H$ (modelled by PYTHIA8) are also included in signal prediction.

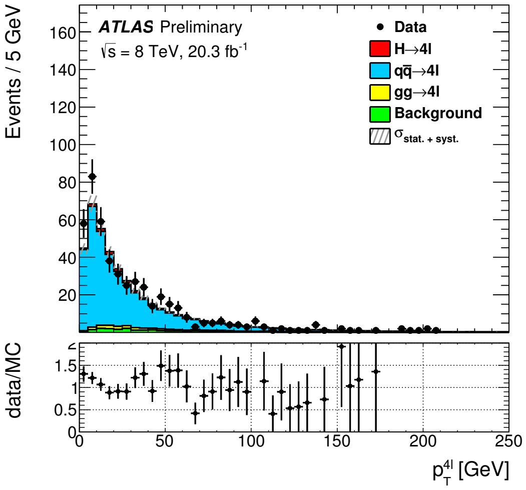

(a)

Figure 9: The transverse momentum p_T distribution of the four-lepton system from data (black points with error bars) and expectations from different 4ℓ signal production processes plus the estimated background contributions (solid colour histograms). Events are selected with full 4ℓ event selection criteria. The expectations of the on-shell Higgs boson (from ggF and VBF processes) and the continuum $q\bar{q} \to ZZ$ productions are modelled with POWHEG-BOX at NLO QCD. The prediction of the non-resonant $gg \to ZZ$ production is calculated with MCFM at the LO. Small contributions from the VBF off-shell Higgs boson and continuum ZZ (modelled by MADGRAPH) and from VH and $t\bar{t}H$ (modelled by PYTHIA8) are also included in signal prediction.

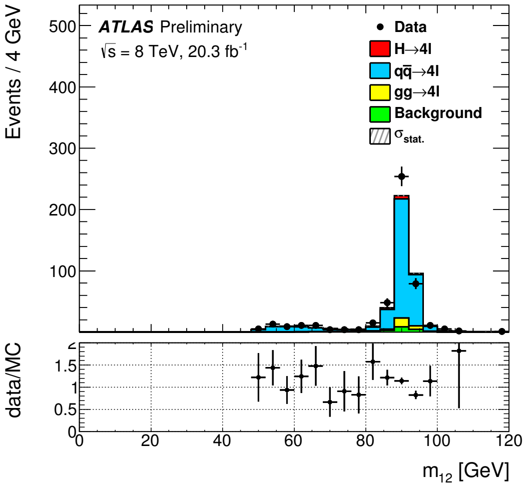

(a)

Figure 10: The leading lepton pair invariant mass distribution from data (black points with error bars) and expectations from different 4ℓ signal production processes plus the estimated background contributions (solid colour histograms). Events are selected with full selection criteria. The expectations of the on-shell Higgs boson and the continuum ZZ productions are modelled with POWHEG-BOX at NLO QCD. The prediction of the non-resonant $gg \rightarrow ZZ$ production is calculated with MCFM at the LO. Small contributions from the VBF off-shell Higgs boson and continuum ZZ (modelled by MADGRAPH) and from VH and $t\bar{t}H$ (modelled by PYTHIA8) are also included in signal prediction.

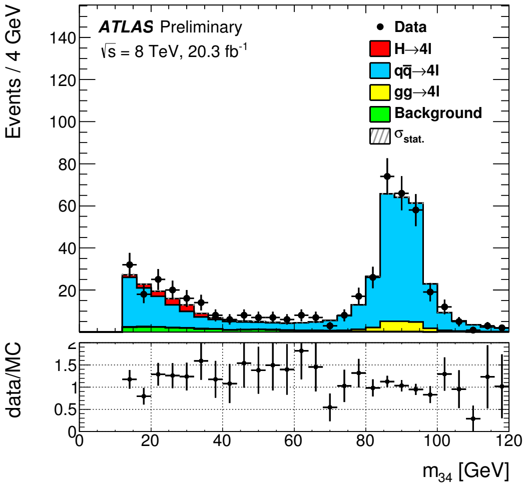

(a)

Figure 11: The subleading lepton pair invariant mass distribution from data (black points with error bars) and expectations from different 4ℓ signal production processes plus the estimated background contributions (solid colour histograms). Events are selected with full selection criteria. The expectations of the on-shell Higgs boson and the continuum ZZ productions are modelled with POWHEG-BOX at NLO QCD. The prediction of the non-resonant $gg \rightarrow ZZ$ production is calculated with MCFM at the LO. Small contributions from the VBF off-shell Higgs boson and continuum ZZ (modelled by MADGRAPH) and from VH and $t\bar{t}H$ (modelled by PYTHIA8) are also included in signal prediction.

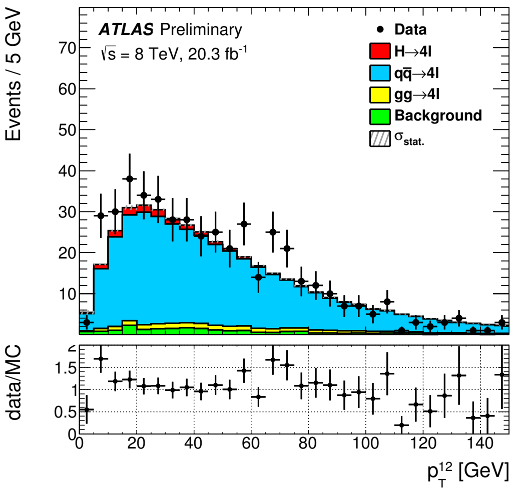

(a)

Figure 12: The transverse momentum p_T distribution of the leading lepton pair from data (black points with error bars) and expectations from different 4ℓ signal production processes plus the estimated background contributions (solid colour histograms). Events are selected with full 4ℓ event selection criteria. The expectations of the on-shell Higgs boson (from ggF and VBF processes) and the continuum ZZ productions are modelled with POWHEG-BOX at NLO QCD. The prediction of the non-resonant $gg \to ZZ$ production is calculated with MCFM at the LO. Small contributions from the VBF off-shell Higgs boson and continuum ZZ (modelled by MADGRAPH) and from VH and $t\bar{t}H$ (modelled by PYTHIA8) are also included in signal prediction.

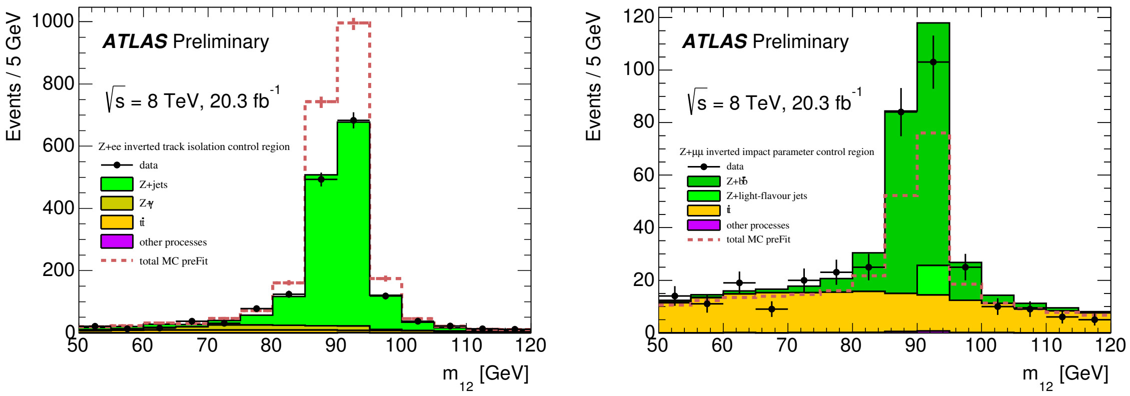

(a) (b)

Figure 13: Control regions used for the estimation of the reducible background. (Left) Inverted track isolation control region used for $\ell\ell + ee$ background. The Z+jets background is generated with SHERPA. (Right) Inverted requirement on impact parameter significance control region used for estimation of $\ell\ell + \mu\mu$ background. The Z+jets background is generated with Alpgen interfaced to PYTHIA. The dotted lines show the total MC expectation before the fit is performed.

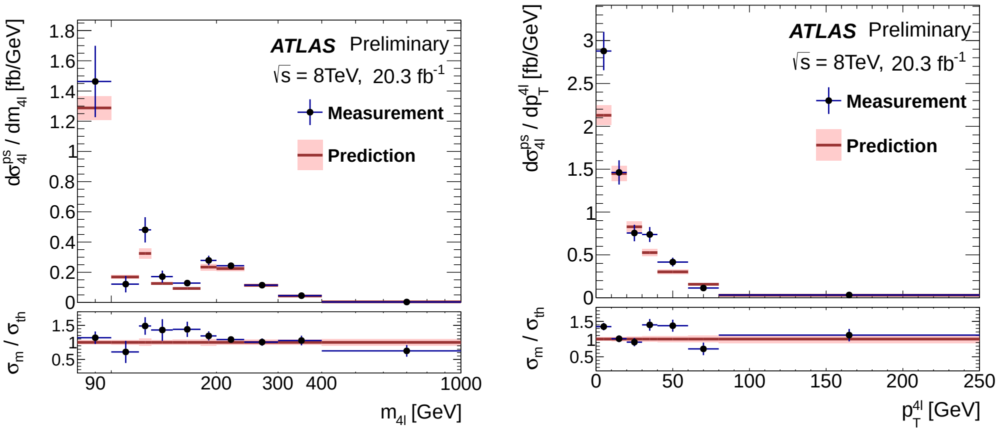

Figure 14: The measured differential cross-section distributions (the black points) of $m_{4\ell}$ (left) and $p_T^{4\ell}$ (right), unfolded in the extended phase space, and compared to theory predictions (red histogram). The combined statistical and systematic uncertainties of the measurements are shown as the error-bars in the unfolded spectra. The theoretical predictions are the sum of the differential cross sections of the $q\bar{q} \rightarrow 4\ell$ and $gg \rightarrow 4\ell$ processes, where the LO cross sections are used for the non-resonant gg-induced signals, while the cross sections of the on-shell Higgs boson and the $q\bar{q}$ productions are corrected with the NNLO K-factors for the $m_{4\ell}$ spectrum; but for $p_T^{4\ell}$, the NLO and LO predictions are used for the $q\bar{q}$ and the gg process, respectively. The total theoretical uncertainties are shown as error bands evaluated by quadratic sum of the contributions from parton showers, QCD scales, PDF sets, and electroweak corrections.